Temperature dependence of Raman and photoluminescence spectra of pure and high-quality MoO3 synthesized by hot wall horizontal thermal evaporation

C. Calvo-Mola, V. Torres-Costa, Y. González, A. Ruediger, M. Sánchez, G. Santana, G. Contreras-Puente, C. de Melo, J. Ghanbaja, D. Horwat, et al.

Journal of Alloys and Compounds
Volume 924, 30 November 2022, 166545

Temperature dependence of Raman and photoluminescence spectra of pure and high-quality MoO_3 synthesized by Hot Wall Horizontal Thermal Evaporation

C. Calvo-Mola,[1] V. Torres-Costa,[2] Y. González,[3] A. Ruediger,[3] M. Sánchez,[1] G. Santana,[4] G. Contreras-Puente,[5] C. de Melo,[6] J. Ghanbaja,[6] D. Horwat, [6] O. de Melo[1,4,*]

[1]Physics Faculty, University of Havana, 10400 La Habana, Cuba

[2]Departamento de Física Aplicada, Universidad Autónoma de Madrid. Cantoblanco 28049, Madrid, Spain

[3]Institut National de la recherche scientifique, Centre Énergie, Matériaux, Télécommunications, 1650 Boulevard Lionel-Boulet, Varennes, Québec, J3X 1S2, Canada

[4]Instituto de Investigaciones en Materiales, Universidad Nacional Autónoma de México, Cd. Universitaria, A.P. 70-360, Coyoacán 04510, México D. F.

[5]Escuela Superior de Física y Matemáticas, Instituto Politécnico Nacional, Mexico City, Mexico,

[6] Institut Jean Lamour, Université de Lorraine, UMR 7198, Nancy F-54000, France

Abstract.

In this work, a novel system for the hot wall evaporation of MoO_3 in a horizontal furnace and at low vacuum atmosphere was settled. Pure MoO_3 material was obtained without the presence of other phases and with a strong preferential orientation, as revealed by electron microscopy, micro-Raman spectroscopy and x-ray diffraction. Photoluminescence and Raman spectra were measured as a function of temperature. As a result, the first-order temperature coefficient of the fifteen measured vibrational modes is reported and compared with the scarce literature data available. The relation

* Corresponding author: odemelo@gmail.com

of these coefficients with the thermal expansion coefficient is discussed in the framework of the Grüneisen model. Moreover, for the first time, the temperature dependence of the different contributions of photoluminescence spectra for MoO_3 is reported, and an anomalous increase in PL intensity of all transitions is observed in the range of 40 to 140 K, followed by a normal quenching at high temperatures. The Shibata model was used to interpret the origin of this anomalous effect.

Keywords: oxide materials, vapor deposition, optical spectroscopy, transmission electron microscopy, phonons

1. Introduction.

The interest in molybdenum oxides has grown considerably in recent years. With a band gap of near 3.0 eV [1] and a large work function, MoO_{3-x} (also called MoO_x, a sub-stoichiometric MoO_3 or a mix of different molybdenum oxide phases) has been used as a hole transporter for both organic [2] and inorganic [3] solar cells. More transparent (and more resistive) stoichiometric MoO_3 is very promising because of its chromic [4] properties, the removal of pollutants in water due to its photocatalytic properties [5], gas sensing ability [6], incorporation in field effect transistors [7] among other applications [8].

Sputtering and Thermal Evaporation (TE) have been frequently used for the growth of the MoO_x films [9–11]. Since the resulting material is usually a mixture of different molybdenum oxide phases, further oxidative treatments [12] are necessary if stoichiometric MoO_3 is required. In addition, in a typically TE process, there is a great loss of source material which, for the most part, ends up deposited in the walls of the evaporation chamber. Also, the uncontrolled heating procedure normally used in TE leads to an often unnecessary increase in source temperature, and high temperature rising of the source, particularly for relatively volatile materials. This prevents a reasonable control of the vapor species and consequently of the stoichiometry of the obtained film. Different Hot Wall evaporation procedures have been developed in an effort to overcome some of the above problems[13].

In this work, we have settled a system for the hot wall evaporation growth of MoO_3 in a horizontal furnace under a low vacuum atmosphere. Unlike the above-mentioned methods, we obtained a pure MoO_3 material without the presence of other phases and with a strong preferential orientation (even when deposited on amorphous glass substrates), as was revealed by scanning electron microscopy (SEM), transmission electron microscopy (TEM), scanning transmission electron

microscopy (STEM), micro-Raman spectroscopy and x-ray diffraction (XRD) techniques. In addition, photoluminescence (PL) and Raman spectra were measured as a function of temperature. While room temperature Raman spectroscopy has been widely used to discriminate between different phases in the Mo-O system, the temperature dependence of Raman spectra has been much less studied. However, it is a powerful tool for investigating the thermal properties of materials and, from a practical point of view, provides a relatively simple, cost-effective, and accurate method for in-situ temperature measurements. This could be very useful in some of the various applications of MoO3. In this paper, we report the first-order temperature coefficient of the fifteen measured vibrational modes, which is compared with the scarce reported data available in the literature in the frame of the Grüneisen model.

The temperature dependence of luminescence is an excellent tool to determine the origin of the different radiative transitions and their relation to the electronic band structure. Thus, the study of the temperature behavior of the energetic position or integrated intensity of relevant luminescent peaks allows differentiation between near-band emission, donor-acceptor pairs and deep centers, for example. In the case of MoO_3, broad room temperature PL spectra covering the visible range have been reported [9–12] by different authors, but, to the best of our knowledge, the temperature dependence of PL has not been studied so far. In the present work, we report an anomalous increase in PL intensity observed for all transitions in the range 40 – 140 K, followed by a normal quenching at higher temperatures. A model, first developed by Shibata [18], was used to determine the parameters involved in the emission.

2. Experimental

MoO_3 powder, used as the source material, was placed in the hottest zone of a horizontal quartz reactor and heated with a tubular furnace to a temperature of 650 ^{o}C. Glass slides or n-type doped

(100) Si, used as substrates, were located in a colder region, around 15 cm far from the source at 180 °C. Using a rotary vacuum pump, the quartz reactor was evacuated to a base pressure of 10^{-3} Torr. Different from chemical vapor deposition, no reactive gases were introduced in the furnace; film growth follows the following steps: thermal sublimation of the source, transport of confined vapor along the horizontal hot walls of the quartz reactor, and deposition in a cooler region (where the temperature is low enough so that the material does not re-vaporize). A temperature controller allowed to set the temperature of the source by means of a thermocouple inserted in the reactor and in close contact with the source. A second thermocouple allowed measuring the substrate temperature. Fig. 1 outlines the set-up for the preparation of the MoO_3 films.

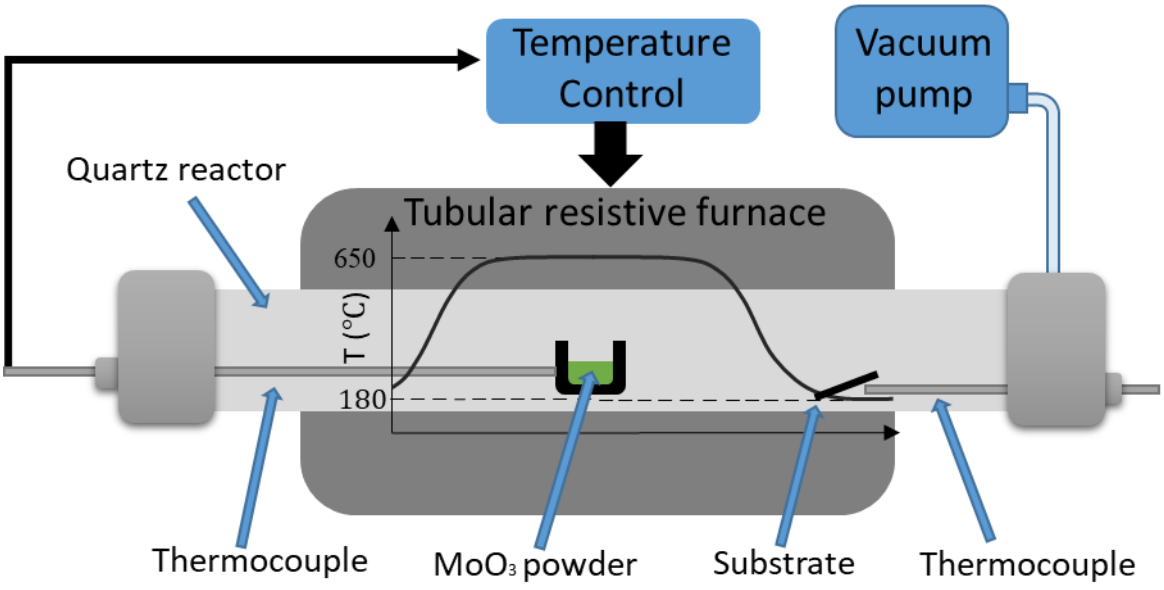

Fig. 1. Schematic of the experimental set-up for the preparation of MoO_3 films, including the temperature profile inside the quartz reactor.

X-ray diffractograms were taken in the $\theta - 2\theta$ configuration using $K_\alpha Cu$ radiation (λ = 1.54 Å) with a Panalytical X-Pert Pro diffractometer. High resolution transmission electron microscopy (HRTEM) and scanning transmission electron microscopy (HRSTEM) measurements were performed by a JEOL

ARM 200-Cold FEG microscope (0.12 nm and 0.078 nm resolution in TEM and STEM mode, respectively). PL spectra were measured by exciting the samples with the 325 nm wavelength line of a He–Cd laser and were corrected considering the spectral response of the system. The sample emission was focused into an Acton SpectraPro 2500i spectrograph and detected by a photomultiplier tube. Raman spectroscopy was carried out with a confocal optical microscope coupled to a modular Raman spectrometer from Horiba (iHR320). The light source was a continuous wave diode-pumped solid-state (CW-DPSS) laser with a wavelength of 473 nm (Cobolt Inc.). The laser was focused onto the sample with a 100 × objective and a power of 2.79 mW. The Raman scattered light was dispersed into the spectrometer with a 2400 lines/mm grating, and a charge-coupled detector (CCD) (Synapse, Horiba Inc.) was used to collect the Raman spectra. SEM images were taken with an FE-SEM Hitachi S-4700 equipment. Surface photovoltage (SPV) measurements were performed at room temperature in a lab-made apparatus[19]; comprising a halogen lamp, a grating monochromator, a lock-in amplifier and an optical chopper. For such measurements, the sample is located between a transparent indium–tin–oxide (ITO) electrode and a copper plate which acts as the sample holder and the bottom ground electrode forming a capacitor. Thus, the SPV signal is capacitively measured via a high-impedance buffer. The signal measured as a function of incident photon energy provides the SPV spectra. The topography exploration was conducted in a SmartSPM1000-AIST-NT Inc atomic force microscope operating in semi-contact mode, using MikroMasch AFM probes (Si) with a tip radius of ~8 nm, a nominal resonant frequency of 325 kHz, and a nominal spring constant of 40 N/m.

3. Results

3.1. Structure and morphology

The orthorhombic crystalline structure of MoO_3 is presented in Fig. 2a. Layers stacked along the b-axis and separated by weak Van der Walls bonds are formed by two sublayers composed by

distorted octahedra rows with O atoms in the vertices and Mo atoms in the center. These sublayers are linked by octahedral vertices/edges in the a-axis/c-axis direction. The three symmetry-distinct O atoms (O1, O2, O3) are represented by different colors (or gray tones in the printed version). As the octahedra are distorted, two different lengths can be observed for the Mo-O2 and Mo-O3 bonds. [20–23]. In Fig. 2b), a x-rays diffractogram (XRD) taken in the $\theta - 2\theta$ configuration (indexed according to the JCPDS card No. 05-0508) of the sample is shown. Room temperature Raman spectrum of an as-grown sample, indexed taking into account previous reports [20–23] is shown in Fig. 2c). Both Raman spectra and XRD results prove that samples are composed of pure MoO_3 without the presence of other MoO_x phases. Moreover, XRD indicates a strong preferential orientation with the (010) crystalline plane parallel to the surface. This orientation is also suggested by the surface morphology, as shown in the SEM image of Fig. 2d). In Fig. 2e) an AFM image shows the height (in nm) of some steps on the surface, including two steps with heights of 0.65 and 0.68 nm, respectively, that correspond with half the b-axis parameter, which is the height of one sublayer.

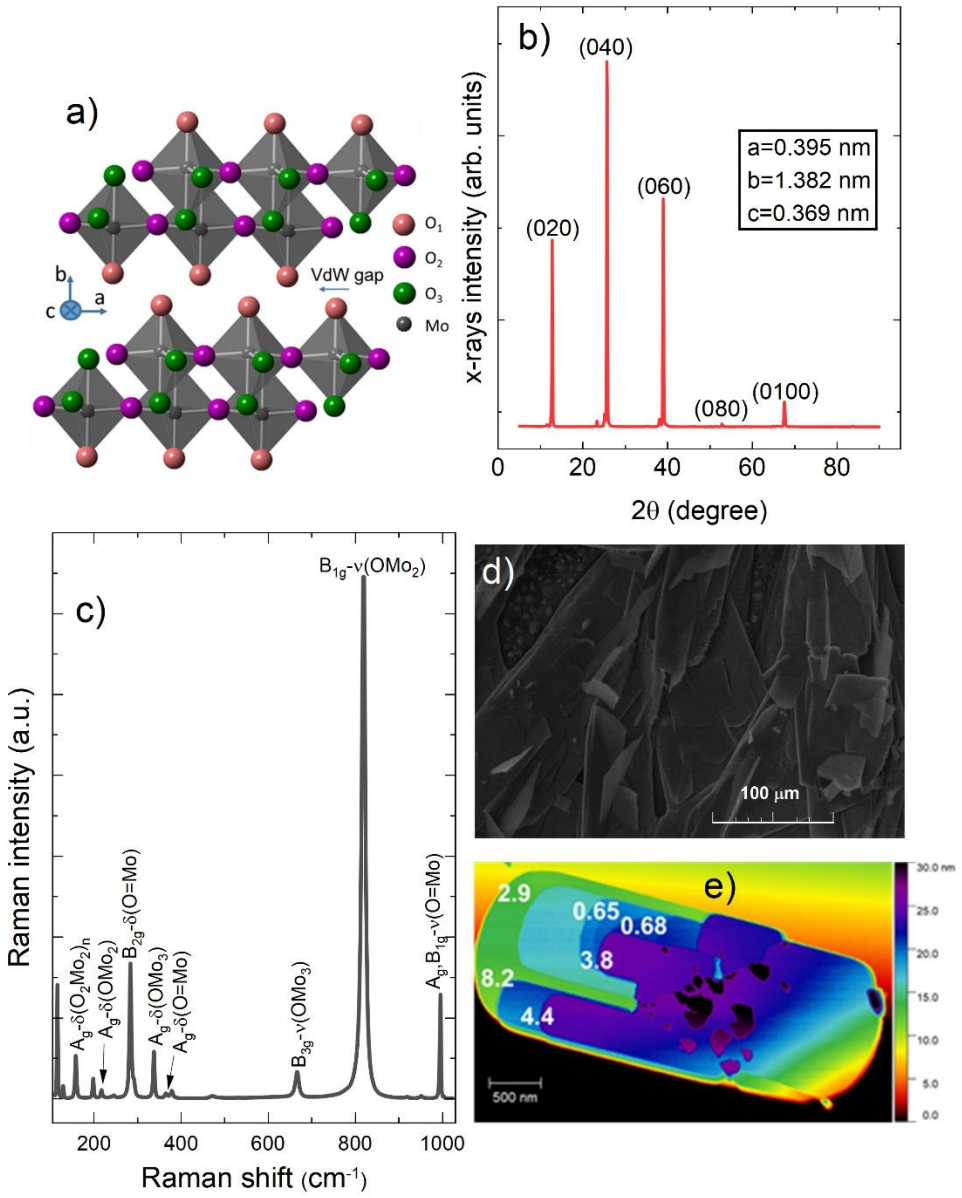

Fig. 2. a) The structure of MoO_3. Layers stacked along the b-axis and separated by weak Van der Walls bonds are formed by two sublayers composed by two distorted octahedra rows with O atoms in the vertices and Mo atoms in the center. The three symmetry-distinct O atoms (O_1, O_2, O_3) are represented by different colors (or gray tones in the printed version). b) X-ray diffractogram of a typical sample grown on soda- lime glass. The large intensity of the (0L0) peaks reflects a high preferential orientation with the [010] direction normal to the surface; c) Raman spectra and d) SEM image of the same sample. The surface morphology, with faceted flakes, suggests confirmation of the preferential orientation; e) AFM image showing the height (in nm) of some steps on the surface. It can be noted that the largest steps are approximately multiples of the lattice parameter b. It is interesting to observe two steps with heights of 0.65 and 0.68 nm, respectively, that correspond with half lattice parameter, which is the height of one sublayer.

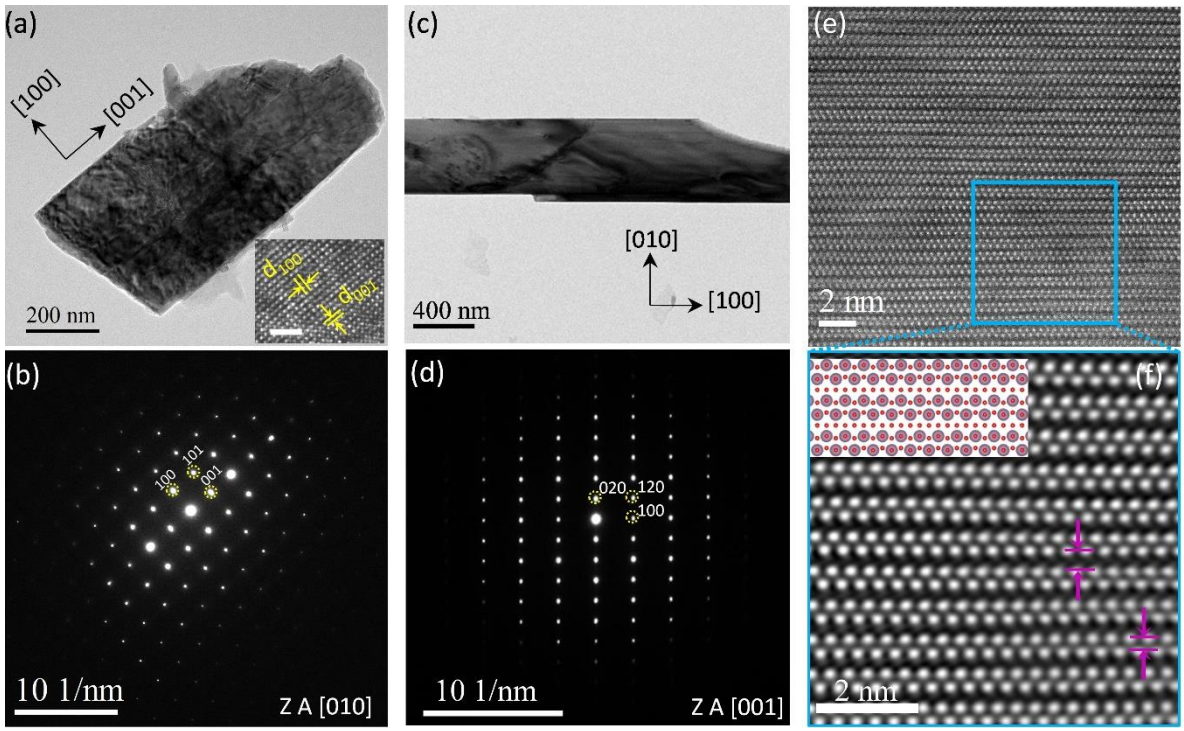

Fig. 3. a) BF-TEM micrograph of a MoO_3 flake grasped from the film surface. In the inset, an HR-TEM micrograph (scale bar of 2 nm) with relevant interplanar distances highlighted: d_{100}=3.72 Å and d_{001}=3.98 Å; b) Indexed selected area electron diffraction pattern for the flake in a) (zone axis [010]); c) and d) BF-TEM micrograph and the corresponding diffraction pattern for a MoO_3 flake found in a different orientation (zone axis [001]); e and f) HAADF-STEM micrographs at two different magnification performed at the MoO_3 flake in c). The simulated MoO_3 structure as viewed in the [001] direction is depicted at the inset of f). The distance between intra and inter-sublayer Mo rows are also displayed.

The bright-field TEM images of two flakes grasped from the films surface and the corresponding selected area diffraction patterns are displayed in Fig. 3 a-d). The two flakes are found to have different orientations: the basal planes are normal to the [010] and [001] directions, respectively. High-angle annular dark-field scanning transmission electron microscopy (HAADF STEM) images showing Mo atoms are presented at two different magnifications in e-f). A simulation of the position of the Mo atoms from the [001] directions is presented in the inset of Fig. f). The intra and inter-sublayer Mo rows in the stacked direction are displayed in f). The different observations did not reveal the presence of point defects, dislocations or stacking faults, indicating that a good crystal quality could be achieved using the proposed synthesis strategy.

3.2. Temperature dependence of the Raman spectra

Fig. 4 shows the evolution with temperature of Raman spectra measured from 100 to 500 °C at 50 °C intervals. The spectra were deconvoluted using 15 Lorentzian functions centered at 114, 127, 154, 197, 215, 243, 282, 290, 336, 364, 377, 472, 667, 819 and 994 cm^{-1}. The peak positions are similar to those reported elsewhere [20,24–26]. In particular it is interesting to note the remarkable coincidence of our measured vibration frequencies with those obtained at ambient pressure for MoO_3 nanoribbons [27] which is an indication of the absence of substrate induced strain on our samples. In Table I, a comparison with previously reported data is shown. It can be easily checked from direct observation that no phase transformation occurs during Raman measurements since no extinction or appearance of any new Raman band could be detected. All the individual peaks show a tendency to red shift with increasing temperature, a characteristic behavior that has been observed in many different materials [28,29]. The change in position $\Delta\omega$ from 100 to 500 °C is shown in column 6 of Table I for each peak. On the other hand, peak shifts with temperature were fitted according to: $\omega(T) = \omega_0 + \chi T$.

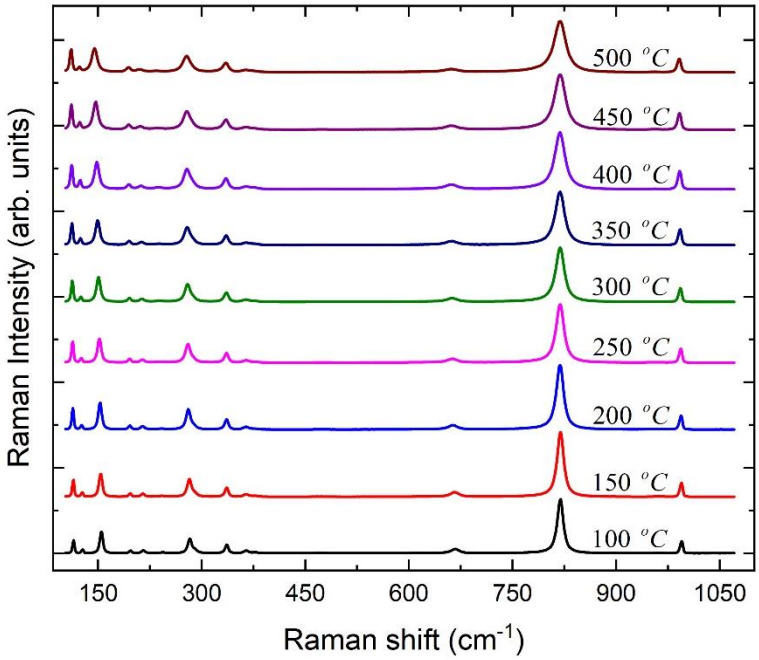

Fig. 4. Temperature evolution of the Raman spectra for a typical MoO_3 sample. It can be observed that there is no extinction or emergence of any Raman band, suggesting the absence of phase transformation in this temperature range.

where ω_0 is the peak position at $0\ K$ and χ, the first-order temperature coefficient [30]. Columns 7 and 8 of Table I show the ω_0 and χ parameters that best fitted the experimental results (the uncertainty of the fit for the most relevant parameter χ is included).

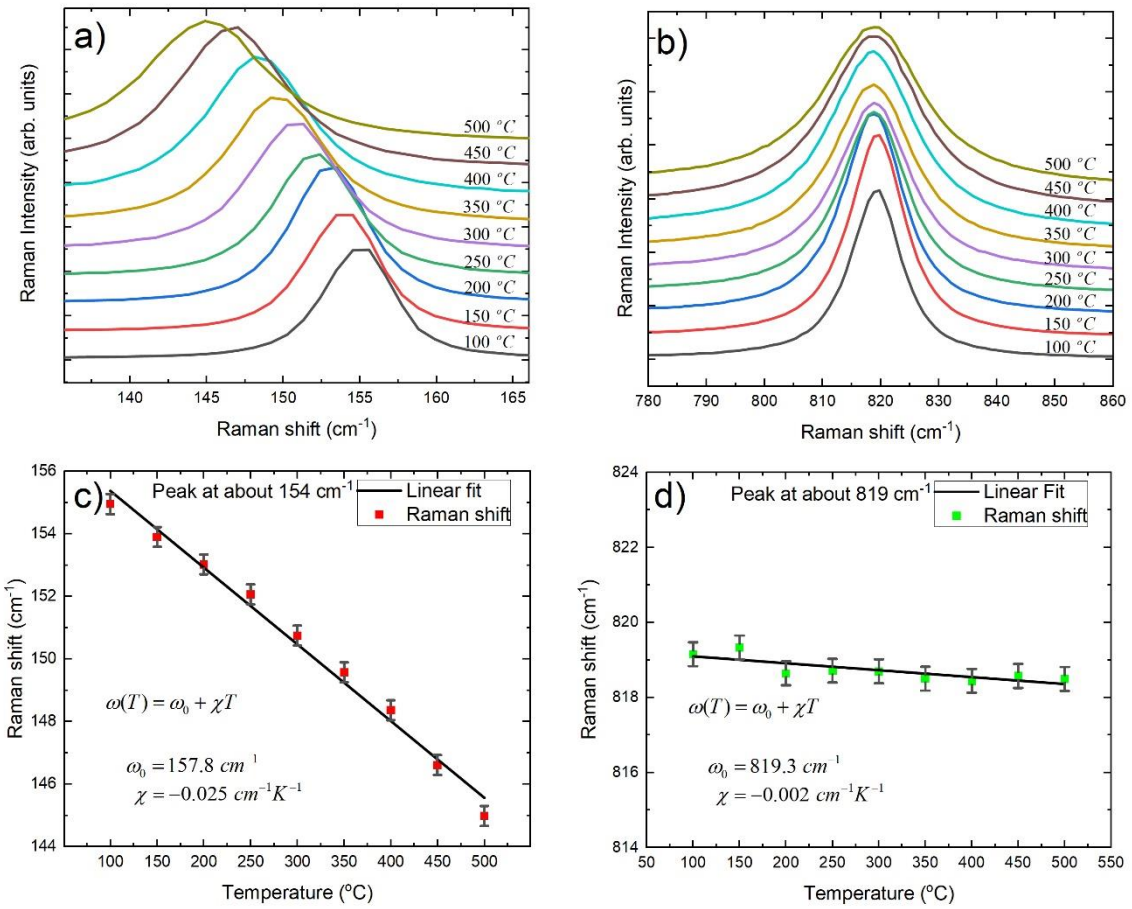

Fig. 5. Temperature evolution of the center of Raman bands near a) 154 cm^{-1} and b) 819 cm^{-1}. Linear fit used to determine the first order Raman coefficient for peaks at about c) 154 cm^{-1} and b) 819 cm^{-1}.

As an example, Figs. 5a) and b) show the evolution with temperature of Raman bands centred at around 154 and 819 cm^{-1}. These figures show the linear fits used to determine the first-order Raman coefficient for the same peaks. The same procedure was carried out for the remaining peaks; it is shown in the supplementary material (S1).

Table I. Raman shifts reported in the literature for MoO_3. $\Delta\omega$ in the range from 100 to 500 ℃ and first-order temperature coefficient of Raman peaks are also presented.

Haro et al. [20] $\omega\,[cm^{-1}]$	Ou et al. [24] $\omega\,[cm^{-1}]$	Camacho et al. [25] $\omega\,[cm^{-1}]$	Atuchin et al. [26] $\omega\,[cm^{-1}]$	This work $\omega\,[cm^{-1}]$	This work $\Delta\omega\,[cm^{-1}]$	This work $\omega_o\,[cm^{-1}]$	This work χ $[10^{-2}cm^{-1}K^{-1}]$
114		112	115	114	-3.6	118	-0.90 ± 0.02
127		124	128	127	-4.9	132	-1.16 ± 0.03
156	154	147	157	154	-9.9	164	-2.49 ± 0.10
196	204	194	197	197	-2.7	199	-0.69 ± 0.02
215		211	217	215	-5.0	221	-1.25 ± 0.06
238		236	245	243	-9.0	251	-2.18 ± 0.07
282	284	280	283	282	-5.3	287	-1.31 ± 0.09
			291	290	-7.4	297	-1.73 ± 0.07
335	333	336	337	336	-1.7	338	-0.43 ± 0.02
363		364	365	364	-0.5	365	-0.11 ± 0.03
	376	376	378	377	-3.6	380	-0.78 ± 0.09
468	471	468	471	472	-0.1	473	-0.10 ± 0.05
		485					
		568					
664	666	662	665	667	-6.2	672	-1.55 ± 0.24
		727					
774							
817	821	819	819	819	-0.7	820	-0.18 ± 0.05
849							
993	995	992	995	994	-3.5	995	-0.91 ± 0.02

Previous measurements of temperature-dependent Raman spectra for MoO_3 in the range 25 – 450 ℃ have been reported in [31], but only the dependence with temperature of the stretching vibration near 998 cm^{-1} (993 cm^{-1} in our work) was presented. Remarkably, the value of χ obtained in that paper agree pretty well with our -0.90 x 10^{-2} $cm^{-1}K^{-1}$ result. In ref. [32] temperature-dependent Raman spectra for MoO_3 nanoribbons in the range 25 – 650 ℃ were measured. They reported frequency-temperature plots only for low wavenumber modes. The range of variation of the frequencies was similar to that of our modes located near 154, 127 and 114 cm^{-1}, but they observed a non-monotonous decrease with a plateau in the range 173 - 350 ℃, which we did not observe at all. They ascribed such behavior to a gradual coalescence process of the nanoribbons as a consequence of the annealing effect.

The frequency variation of the Raman modes with temperature is due to an anharmonic behavior leading to cell expansion with increasing temperatures [33]. It is characterized by the Grüneisen parameter, which, for the i-th vibrational mode, is defined as [34]:

$$\gamma_i = \frac{\partial(\log \omega_i)}{\partial(\log V)} \tag{1.1}$$

In this expression ω_i is the frequency of the i-th mode, and V is the cell volume. Following thermodynamic considerations, the relative rate of change of frequency with temperature $\frac{1}{\omega_i}\frac{d\omega_i}{dT}$ can be expressed as:

$$\frac{1}{\omega_i}\frac{d\omega_i}{dT} = -\gamma_i \beta \tag{1.2}$$

Where β is the coefficient of thermal expansion, and γ_i is in general different for each mode. In the case of isotropic thermal expansion, a weighted average of the different γ_i can be used. However, in the case of MoO_3, it has been found that the thermal expansion coefficient is strongly anisotropic [35,36], the linear expansion along the b axis (the axis normal to the stacked lamellae) being much higher than along the other axes.[†] Furthermore, in ref. [36], based on x-ray diffraction measurements, the authors have found a negative thermal expansion coefficient along the c-axis. In our measurements, $\frac{1}{\omega_i}\frac{d\omega_i}{dT}$ results in negative values for all modes; this indicates that Grüneisen parameters and expansion coefficients have the same sign. We used the linear expansion coefficients reported in the literature cited above [36] to determine the Grüneisen parameter from our χ value for the stretching vibrations along the lattice vector directions *a, b, c* (819, 994 and 667 cm^{-1}, respectively). The results are shown in Table II together with the used linear expansion coefficient and the Grüneisen parameter reported in [36]. Significant quantitative disagreement is

[†] The arrangement of the lattice vectors in our work is different than in that reference: our a, b, c lattice vectors, represent the c, a, b lattice vectors in the cited article.

observed between our results and those of that reference, which is probably due to the fact that our approximation is too simplified since only the stretching vibrations were considered. On the other hand, in reference 33, it was observed that the thermal expansion along the b axis is rather determined by the increase of the Van der Waals gap distance and not by the Mo-O bond: the relation between the thermal expansion of the Mo-O bond with respect to that of the Van der Waals gap was found to be 1/10. This effect could explain a lower mode frequency dependence and an underestimation of the Grüneisen parameter along the b axis. In fact, if we consider that the actual expansion coefficient for the Mo-O bond is 1/10 of the measured expansion coefficient along this direction, the calculated γ_i will approximately approach the value of 2, which compares with the value of 3.2 reported in [36]. A similar, no homogeneous distribution of the expansion coefficient in the other directions would partly explain the observed discrepancies. At all, a theoretical estimation of the Grüneisen parameter along the different directions would be needed for each vibration mode to get a better understanding of the relation between the χ values reported in the present work, the linear expansion coefficients β, and the Grüneisen parameter γ_i. The values reported here can be useful for this kind of studies.

Table II. Comparison of the Gruneisen parameter calculated in ref. 33 from a fit of the temperature dependence of the linear thermal expansion and our calculations from the frequency Raman modes-temperature dependence.

Direction *a, b, c*	Mean value of the linear expansión coefficients β (K^{-1}) (ref. 33)	Grüneisen parameter γ_i ref. 33	Frecuency ω_i (cm^{-1})	χ ($cm^{-1}K^{-1}$) (this work)	$\gamma_i = -\frac{1}{\beta}\frac{1}{w_i}\chi$ (this work)
A	1.0×10^{-5}	18	819	-0.002	0.24
B	4.5×10^{-5}	3.4	994	-0.009	0.20/2*
C	-0.35×10^{-5}	-20	667	-0.015	-6.4

*Considering a smaller thermal expansion coefficient as explained in the text

3.2 Photoluminescence temperature dependence

The temperature dependence of the photoluminescence spectra (in the range 12 -290 K) for a typical MoO_3 sample is presented in Fig. 5. Spectra is quite broad over the whole visible range. At low temperatures, a white luminescence was observed while, for temperatures above 180 K, a green shift of the whole spectrum was observed. All PL spectra were deconvoluted using five Gaussian contributions centred at 2.09, 2.68, 2.90, 3.02, and 3.09 eV in the 12 K spectra, as shown in Fig. 6a) displays, as an example. Fig 6b) shows the evolution of the center of the deconvoluted Gaussians with temperature.

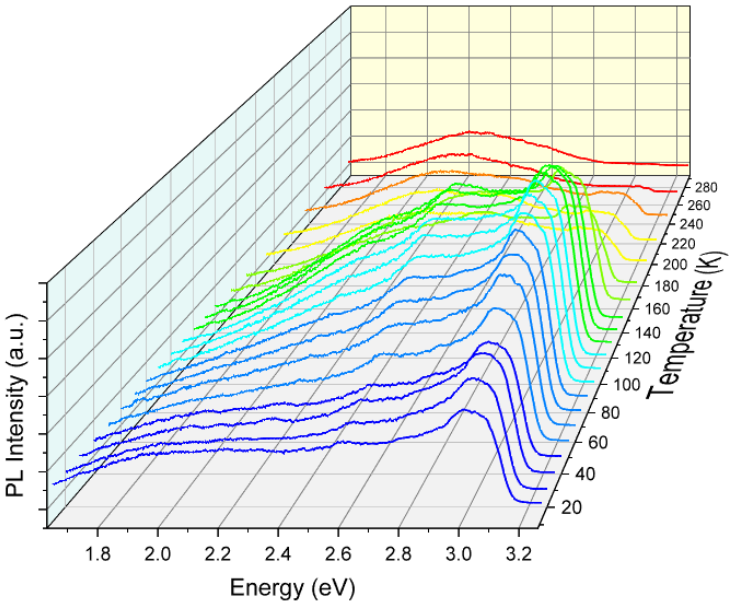

Fig. 5. Photoluminescence spectra of the MoO3 samples as a function of temperature.

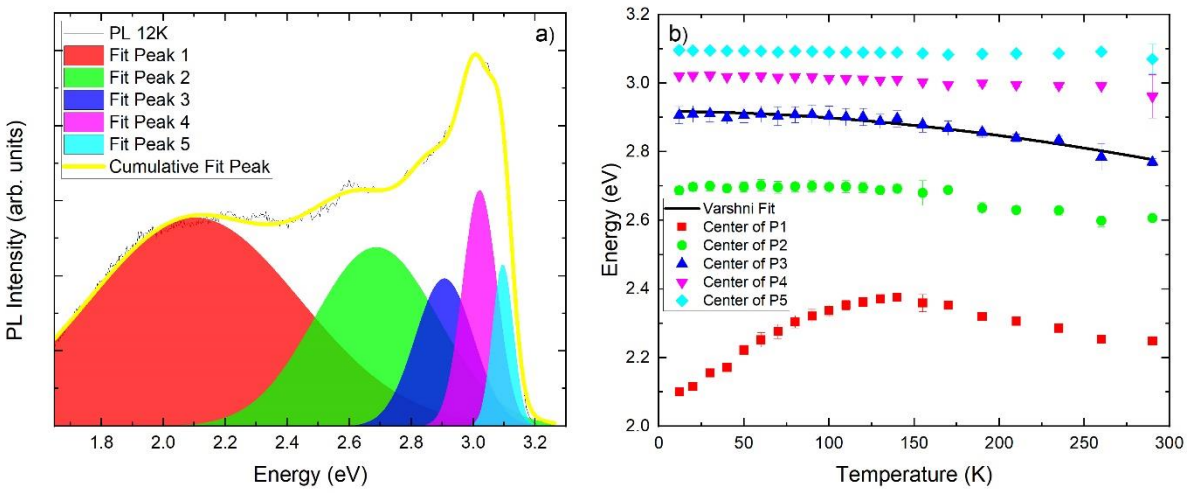

Fig. 6. a) Pl spectra of a MoO_3 sample at 12 K deconvoluted using five Gaussian contributions centred at 2.09, 2.68, 2.90, 3.02, 3.09 eV, respectively. b) Evolution with temperature of the center of Gaussian contribution. (Varshni empirical equation fit is shown with a solid line).

Several authors reported the band gap of MoO_3 at around 3 eV [8,37–39]. The peak 3 (2.90 eV at low temperature) presents the typical shrinkage with increasing temperature of near band edge emissions (NBE) which we have fitted by the semi-empirical Varshni equation [40]:

$$E_{PL}(T) = E_{PL}(0) - \frac{\alpha T^2}{\beta + T} \qquad (1.3)$$

With $\alpha = 3.0\ meV\ K^{-1}$ and $\beta = 1.51\ x\ 10^3\ K$. $E_{PL}(0)$ is the emission peak position at 0 K and T is the absolute temperature. Such a fitting is shown by a solid line in Fig. 6b.

It is interesting to note that the position of the higher energy peaks at 3.02 and 3.09 eV remains practically unchanged with increasing temperature. These emission bands have been associated with $(d_{z^2} - d_{yz})$ split transition in an octahedral crystal field [41] after the analysis of diffuse reflectance spectra. Crystal field splitting excitation, common to transition metals bound to ligands, has also been observed for MoO_3 in [42], using electron paramagnetic resonance measurements.

The energy location and temperature behavior in our PL spectra seem to support the above assumptions.

The peak located at 2.68 eV barely changes its center with increasing temperature. This emission band is probably due to a point defect or donor-acceptor pair. Transition at circa 2.0 eV at low temperature is expected to be related with a deep level within the band gap.

Evolution with temperature of the intensities of PL bands is shown in Fig. 7. All PL bands show similar qualitative behavior: up to 40 K, the intensity remains approximately unchanged, while for temperatures higher than 140 K, a thermal quenching is observed. In the range 40-140 K, they experience an anomalous increase in intensity. The fact that all the bands show an increase in the intensity over a similar temperature range seems to exclude the presence of the Schön-Klasens or multi-center mechanism, according to which the increase in the intensity of some transitions occurs at the expense of the quenching of others [43]. Similar anomalous behavior has been observed in other materials [44,45], often referred to as negative thermal quenching (NTQ), and is commonly associated with thermal release of carriers at traps or localized surface states [46]. In [40], dissociation of an exciton with the injection of free electrons in the conduction band serves as an additional source for the conduction band- acceptor transitions which present NTQ in ZnO nanocrystals. In [39], the red band (deep donor-deep acceptor transition) of GaN present NTQ because of the thermal excitation of electrons from a shallow donor to the conduction band. On the other hand, in [41], surface trap levels in ZnO nanostructures are responsible for directly feeding the initial state of both free exciton and green transition, with two different activation energies.

The NTQ of luminescence can be explained by a model developed by Shibata et al [18]. For the most general case of PL, intensity can be fitted using Shibata's model equation as:

$$I(T) = I(0) + \frac{1 + \sum_{q=1}^{w} D_q \exp(-E'_q / k_B T)}{1 + \sum_{j=1}^{m} C_j \exp(-E_j / k_B T)} \qquad (1.4)$$

where k_B is the Boltzmann constant, $I(0)$ correspond to PL intensity at absolute cero, D_q and C_j are parameters associated with radiative and non-radiative mechanisms, respectively, E'_q and E_j are the energy of activation of the negative and the normal thermal quenching, respectively. In the simplest case, only one mechanism is considered for each contribution and equation (1.2) takes the form:

$$I(T) = I(0) + \frac{1 + D \exp(-E' / k_B T)}{1 + C \exp(-E / k_B T)} \qquad (1.5)$$

The solid lines in Fig. 7 show the fit for each PL band using (*1.5*). The best-fit parameters obtained are shown in Table II.

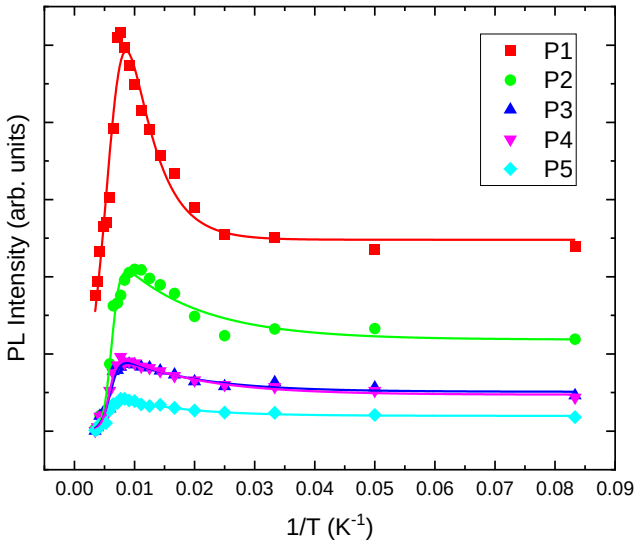

Fig. 7. PL intensities evolution with the inverse of the absolute temperature (solid symbols) and Shibata model fit to the data points (lines). Fitting parameters are reported in Table II for each PL peak.

Table II. Best-fit Shibata model parameters for the different contributions of the luminescence. E' and E correspond with activation energy of increase PL and thermal quenching activation energy, respectively. D and C are fit parameters.

	D	E'	C	E
Peak 1	10.14	$19 \pm 5.1\ meV$	83.07	$58 \pm 5\ meV$
Peak 2	1.49	$6.4 \pm 2.3\ meV$	$1.1 \cdot 10^4$	$128 \pm 21\ meV$
Peak 3	1.55	$6.7 \pm 2.8\ meV$	$2.2 \cdot 10^3$	$110 \pm 18\ meV$
Peak 4	1.86	$6.4 \pm 1.4\ meV$	$7.9 \cdot 10^3$	$131 \pm 15\ meV$
Peak 5	2.4	$8.0 \pm 1.8\ meV$	$5.0 \cdot 10^3$	$126 \pm 15\ meV$

It can be observed that peaks 2-5 show approximately the same activation energy of NTQ (6-8 meV). If the NTQ is due to direct feeding of the initial state of the transitions, this suggests that all the transitions have the initial state at the same energy (if the initial states were different for the different transitions, a feeding state located 6-8 meV below every initial state does not seem to be a realistic assumption). If the NTQ is due to indirect feeding of electrons to the conduction band with subsequent relaxation to the initial state of each transition, the initial states may be located at different energies, and the feeding state should be 6-8 meV below the conduction band minimum and would be a neutral shallow donor.

The activation energy of the standard thermal quenching of PL is also of the same order for these transitions. It is probably a consequence of all the transitions having the same non-radiative quenching mechanism, probably a relatively deep acceptor level (taking into account the n-type condition of MoO_3). Since the MoO_3 is expected to have an indirect band gap, we suppose that, in this relatively intense luminescence, defect states are involved rather than band-to-band or free exciton emission. In fact, NBE assigned peak 3 presents a low-temperature energy position which is smaller than the band gap energy by about 100 meV. This points to a defect-band transition (donor-acceptor transition can be excluded because they are not expected to follow the temperature shrinkage of the gap and are not considered as NBE transitions). However, a complete interpretation of the origin of the different PL bands is rather difficult since it is hard to explain that the same

negative thermal quenching activation energy exists for transitions of a different nature as crystal field splitting levels or band states. A reasonable explanation could be considered a slightly higher than 3 eV band gap. In such a way, crystal field splitting levels could be fed from the conduction band due to the ionization of a shallow level located at around 6 meV below the conduction band, thereby explaining the NTQ behavior.

3.3 Surface photovoltage spectroscopy

Surface photovoltage spectroscopy (SPS) is a particularly useful technique to study the electronic transition caused by the light absorption in semiconductors [47]. Figure 10 shows an SPV spectra (black line) for one of the MoO_3 samples obtained with this method. Details on the experimental procedure can be seen in reference [19]. In SPS, electronic transitions are associated with changes in the slope of the SPV spectra. The energy value of the transitions can be clearly obtained from the derivative spectra $d(E{\cdot}SPV)/dE$ (red line), also included in the figure. The maxima, corresponding to the inflection points in the original spectrum, give the energy positions of the electronic transitions observed in the original spectrum. Two main bands are clearly observed. The relatively wide band at around 3.08 eV can be related with the higher energies PL emission peaks observed in the region of the band gap [1,37,48] (peaks 1-3 in Fig. 6). Since SPS, in general, resembles the absorption spectrum this is a reasonable explanation. Transition at 2.38 eV has been commonly associated with defect states, presumably oxygen vacancies or Mo^{5+} centers [41,49] and may be related to the PL transitions 5, 6 in Fig. 6.

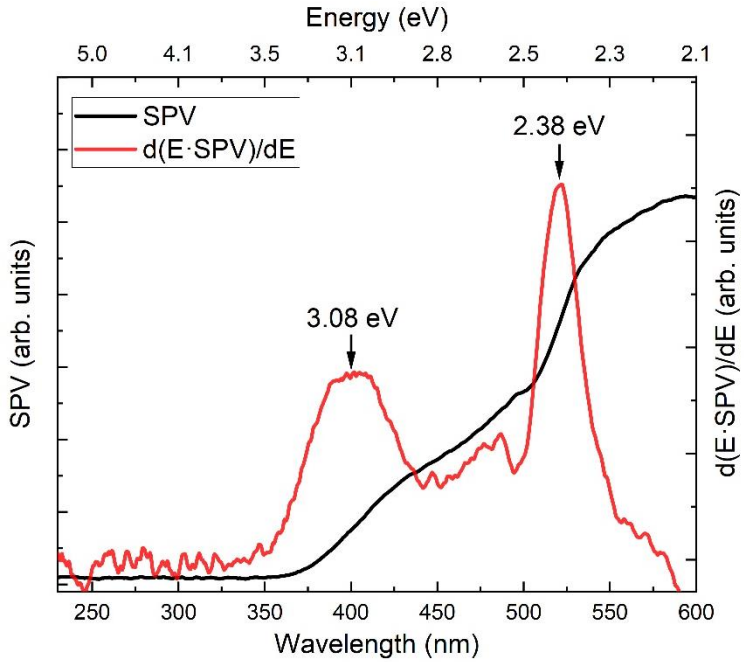

Fig. 10. SPV spectra (black) and $\mathbf{d(E \cdot SPV)/dE}$ (red) of a typical MoO3 sample. The graph shows transitions related to a near-bandgap (3.08 eV) and an inter-band defect state (2.38 eV).

4. Conclusions

Using a simple hot wall thermal evaporation system in horizontal configuration and under low vacuum conditions, strongly oriented pure MoO_3 films with the b-axis normal to the surface were grown on glass substrates. Raman spectra and x-ray diffraction analysis showed that no spurious phases were present. Very thin single crystal flakes were exfoliated from the films, and the crystal structure of MoO_3 was verified in two different zone axes by means of high-resolution TEM images and electron diffraction patterns. High resolution STEM confirmed the high quality of the synthesized MoO_3 film.

Temperature dependence of Raman spectra allowed to report the first order temperature coefficient of the frequencies for the fifteen vibrational modes measured. The relation of this coefficient with the thermal expansion coefficient reported in the literature was discussed according to the Grüneisen treatment for anharmonicity. Since the thermal expansion coefficient of MoO_3 is

anisotropic and inhomogeneous along the different directions, the interpretation of the parameters guiding the thermal expansion is not trivial but very important for applications such as heterostructures, or atoms intercalation, for example. The first-order temperature coefficients reported here may help to a better understanding of this thermal phenomenon.

The temperature dependence of the photoluminescence contributions of MoO_3 is reported for the first time for MoO_3. The observed transitions were identified according to their temperature behavior and considering previous reports on the optical properties of MoO_3. Thus, the more energetic transitions were associated with $(d_{z^2} - d_{yz})$ split in an octahedral crystal field. A transition at lower energy was found to have the typical qualitative band gap thermal evolution and was fitted with the Varshni equation typically used for band gap related emissions. As the low temperature value of this emission is appreciably smaller than that reported for the band gap of MoO_3, we consider this emission as a near band edge one. Then, apart from a constant offset value, it is the first report of the temperature dependence of the MoO_3 band gap. A negative thermal quenching was observed in the range of 40 – 140 K for all the transitions, followed by a normal quenching at higher temperatures. Shibata's model, which has been used to interpret the negative thermal quenching of the luminescence in other materials, allowed to fit the temperature dependence of the intensity for the different transitions. Similar activation energies of about 6 meV were found for the NTQ in the four more energetic transitions. We hypothesize that the ionization of a shallow donor, with ionization energy of about 6 meV, and subsequent relaxation to the initial states of the transitions are responsible for the negative thermal quenching of the photoluminescence.

In addition to proposing a new and simple preparation method for pure MoO_3 layers, this work is a contribution to the understanding of the thermal and optical properties of MoO_3, a very versatile material with potential applications in several branches of technology.

Acknowledgements. OdM and GS thanks the support of UNAM/DGAPA/PREI program 2021. This work was partly funded by the Community of Madrid within the framework of the agreement with Universidad Autonoma de Madrid in item “Excellence of University Professorate”

References

[1] O. de Melo, Y. González, A. Climent-Font, P. Galán, A. Ruediger, M. Sánchez, C. Calvo-Mola, G. Santana, V. Torres-Costa, Optical and electrical properties of MoO2 and MoO3 thin films prepared from the chemically driven isothermal close space vapor transport technique, J. Phys.: Condens. Matter. 31 (2019) 295703. https://doi.org/10.1088/1361-648X/ab18e2.

[2] R. Liu, S.-T. Lee, B. Sun, 13.8% Efficiency hybrid Si/organic heterojunction solar cells with MoO3 film as antireflection and inversion induced layer, Adv Mater. 26 (2014) 6007–6012. https://doi.org/10.1002/adma.201402076.

[3] L.G. Gerling Sarabia, S. Mahato, A.B. Morales-Vilches, G. Masmitjà Rusiñol, P.R. Ortega Villasclaras, C. Voz Sánchez, R. Alcubilla González, J. Puigdollers i González, Transition metal oxides as hole-selective contacts in silicon heterojunctions solar cells, Solar Energy Materials and Solar Cells. 145 (2016) 109–115. https://doi.org/10.1016/j.solmat.2015.08.028.

[4] T. He, J. Yao, Photochromism of molybdenum oxide, Journal of Photochemistry and Photobiology C: Photochemistry Reviews. 4 (2003) 125–143. https://doi.org/10.1016/S1389-5567(03)00025-X.

[5] W. Wei, Z. Zhang, G. You, Y. Shan, Z. Xu, Preparation of recyclable MoO3 nanosheets for visible-light driven photocatalytic reduction of Cr(VI), RSC Adv. 9 (2019) 28768–28774. https://doi.org/10.1039/C9RA05644K.

[6] D. Kwak, M. Wang, K.J. Koski, L. Zhang, H. Sokol, R. Maric, Y. Lei, Molybdenum Trioxide (α-MoO3) Nanoribbons for Ultrasensitive Ammonia (NH3) Gas Detection: Integrated Experimental and Density Functional Theory Simulation Studies, ACS Appl. Mater. Interfaces. 11 (2019) 10697–10706. https://doi.org/10.1021/acsami.8b20502.

[7] M.M.Y.A. Alsaif, A.F. Chrimes, T. Daeneke, S. Balendhran, D.O. Bellisario, Y. Son, M.R. Field, W. Zhang, H. Nili, E.P. Nguyen, K. Latham, J. van Embden, M.S. Strano, J.Z. Ou, K. Kalantar-zadeh, High-Performance Field Effect Transistors Using Electronic Inks of 2D Molybdenum Oxide Nanoflakes, Advanced Functional Materials. 26 (2016) 91–100. https://onlinelibrary.wiley.com/doi/abs/10.1002/adfm.201503698 (accessed February 5, 2021).

[8] I.A. de Castro, R.S. Datta, J.Z. Ou, A. Castellanos-Gomez, S. Sriram, T. Daeneke, K. Kalantar-zadeh, Molybdenum Oxides – From Fundamentals to Functionality, Advanced Materials. 29 (2017) 1701619. https://doi.org/10.1002/adma.201701619.

[9] M. Bivour, F. Zähringer, P. Ndione, M. Hermle, Sputter-deposited WOx and MoOx for hole selective contacts, Energy Procedia. 124 (2017) 400–405. https://doi.org/10.1016/j.egypro.2017.09.259.

[10] F.M.T. Mendes, D.E. Weibel, R.-P. Blum, J. Middeke, M. Hafemeister, H. Niehus, C.A. Achete, Preparation and characterization of well-ordered MoOx films on Cu3Au(100)–oxygen substrate (CAOS), Catalysis Today. 133–135 (2008) 187–191. https://doi.org/10.1016/j.cattod.2007.11.046.

[11] B. Macco, M.F.J. Vos, N.F.W. Thissen, A.A. Bol, W.M.M. Kessels, Low-temperature atomic layer deposition of MoOx for silicon heterojunction solar cells, Physica Status Solidi (RRL) – Rapid Research Letters. 9 (2015) 393–396. https://doi.org/10.1002/pssr.201510117.

[12] M.F. Al-Kuhaili, S.M.A. Durrani, I.A. Bakhtiari, Pulsed laser deposition of molybdenum oxide thin films, Appl. Phys. A. 98 (2010) 609–615. https://doi.org/10.1007/s00339-009-5444-3.

[13] D. Stifter, H. Sitter, Hot wall epitaxy of C60 thin films on mica, Appl. Phys. Lett. 66 (1995) 679–681. https://doi.org/10.1063/1.114097.

[14] R.K. Sharma, G.B. Reddy, Controlled growth of vertically aligned MoO3 nanoflakes by plasma assisted paste sublimation process, Journal of Applied Physics. 114 (2013) 184310. https://doi.org/10.1063/1.4830278.
[15] B.B. Wang, X.X. Zhong, B.M. Ming, M.K. Zhu, Y.A. Chen, U. Cvelbar, K. Ostrikov, Structure and photoluminescence properties of MoO3−x/graphene nanoflake hybrid nanomaterials formed via surface growth, Applied Surface Science. 480 (2019) 1054–1062. https://doi.org/10.1016/j.apsusc.2019.02.183.
[16] B.B. Wang, X.X. Zhong, R.W. Shao, Y.A. Chen, U. Cvelbar, K. Ostrikov, Effects of tungsten doping on structure and photoluminescence of MoO3–x nanomaterials, J. Phys. D: Appl. Phys. 53 (2020) 415109. https://doi.org/10.1088/1361-6463/ab9ad6.
[17] Y. Chen, B. Wang, Effects of deposition parameters on structures and photoluminescence of MoO3-x nanomaterials grown by CVD, Optical Materials. 92 (2019) 150–155. https://doi.org/10.1016/j.optmat.2019.04.010.
[18] H. Shibata, Negative Thermal Quenching Curves in Photoluminescence of Solids, Jpn. J. Appl. Phys. 37 (1998) 550. https://doi.org/10.1143/JJAP.37.550.
[19] Y. González, A. Abelenda, O. de Melo, C. Calvo-Mola, L. García-Pelayo, B.J. García, M. Sánchez, Automated system for surface photovoltage spectroscopy, Review of Scientific Instruments. 92 (2021) 013104. https://doi.org/10.1063/5.0035179.
[20] E. Haro-Poniatowski, C. Julien, B. Pecquenard, J. Livage, M.A. Camacho-López, Laser-induced structural transformations in MoO3 investigated by Raman spectroscopy, Journal of Materials Research. 13 (1998) 1033–1037. https://doi.org/10.1557/JMR.1998.0144.
[21] L. Seguin, M. Figlarz, R. Cavagnat, J.-C. Lassègues, Infrared and Raman spectra of MoO3 molybdenum trioxides and MoO3 · xH2O molybdenum trioxide hydrates, Spectrochimica Acta Part A: Molecular and Biomolecular Spectroscopy. 51 (1995) 1323–1344. https://doi.org/10.1016/0584-8539(94)00247-9.
[22] M.A. Py, K. Maschke, Intra- and interlayer contributions to the lattice vibrations in MoO 3, Physica B+C. 105 (1981) 370–374. https://doi.org/10.1016/0378-4363(81)90278-3.
[23] O. de Melo, F. Agulló-Rueda, V. Torres-Costa, Spatially resolved MoOx phases by the laser oxidation of MoO2: a possible route for all-molybdenum oxide devices, J. Mater. Chem. C. 9 (2021) 6579–6588. https://doi.org/10.1039/D1TC00696G.
[24] J.Z. Ou, J.L. Campbell, D. Yao, W. Wlodarski, K. Kalantar-zadeh, In Situ Raman Spectroscopy of H2 Gas Interaction with Layered MoO3, J. Phys. Chem. C. 115 (2011) 10757–10763. https://doi.org/10.1021/jp202123a.
[25] M.A. Camacho-López, L. Escobar-Alarcón, M. Picquart, R. Arroyo, G. Córdoba, E. Haro-Poniatowski, Micro-Raman study of the m-MoO2 to α-MoO3 transformation induced by cw-laser irradiation, Optical Materials. 33 (2011) 480–484. https://doi.org/10.1016/j.optmat.2010.10.028.
[26] V.V. Atuchin, T.A. Gavrilova, T.I. Grigorieva, N.V. Kuratieva, K.A. Okotrub, N.V. Pervukhina, N.V. Surovtsev, Sublimation growth and vibrational microspectrometry of α-MoO3 single crystals, Journal of Crystal Growth. 318 (2011) 987–990. https://doi.org/10.1016/j.jcrysgro.2010.10.149.
[27] J.V. Silveira, L.L. Vieira, A.L. Aguiar, P.T.C. Freire, J. Mendes Filho, O.L. Alves, A.G. Souza Filho, Pressure-induced phase transition and fracture in α-MoO3 nanoribbons, Spectrochimica Acta Part A: Molecular and Biomolecular Spectroscopy. 193 (2018) 47–53. https://doi.org/10.1016/j.saa.2017.11.053.
[28] S. Luo, X. Qi, H. Yao, X. Ren, Q. Chen, J. Zhong, Temperature-Dependent Raman Responses of the Vapor-Deposited Tin Selenide Ultrathin Flakes, J. Phys. Chem. C. 121 (2017) 4674–4679. https://doi.org/10.1021/acs.jpcc.6b12059.

[29] D. Lu, S. Luo, S. Liu, H. Yao, X. Ren, W. Zhou, D. Tang, X. Qi, J. Zhong, Anomalous Temperature-Dependent Raman Scattering of Vapor-Deposited Two-Dimensional Bi Thin Films, J. Phys. Chem. C. 122 (2018) 24459–24466. https://doi.org/10.1021/acs.jpcc.8b07957.
[30] T. M, D.J. Late, Temperature Dependent Phonon Shifts in Single-Layer WS2, ACS Appl. Mater. Interfaces. 6 (2014) 1158–1163. https://doi.org/10.1021/am404847d.
[31] S. Xie, E. Iglesia, A.T. Bell, Effects of Temperature on the Raman Spectra and Dispersed Oxides, J. Phys. Chem. B. 105 (2001) 5144–5152. https://doi.org/10.1021/jp004434s.
[32] J.V. Silveira, L.L. Vieira, J.M. Filho, A.J.C. Sampaio, O.L. Alves, A.G. Souza Filho, Temperature-dependent Raman spectroscopy study in MoO3 nanoribbons, Journal of Raman Spectroscopy. 43 (2012) 1407–1412. https://doi.org/10.1002/jrs.4058.
[33] G. Lucazeau, Effect of pressure and temperature on Raman spectra of solids: anharmonicity, Journal of Raman Spectroscopy. 34 (2003) 478–496. https://doi.org/10.1002/jrs.1027.
[34] A. Schauer, Thermal expansion of solids and the temperature dependence of lattice vibration frequencies, Can. J. Phys. 42 (1964) 1857–1864. https://doi.org/10.1139/p64-173.
[35] P. KIERKEGAARD, Differential thermal analysis of vanadium pentoxide, and thermal expansion of molybdenum trioxide and vanadium pentoxide, ARKIV FOR KEMI. 23 (1965) 223.
[36] H. Negishi, S. Negishi, Y. Kuroiwa, N. Sato, S. Aoyagi, Anisotropic thermal expansion of layered MoO3 crystals, Phys. Rev. B. 69 (2004) 064111. https://doi.org/10.1103/PhysRevB.69.064111.
[37] M.A. Bica de Moraes, B.C. Trasferetti, F.P. Rouxinol, R. Landers, S.F. Durrant, J. Scarmínio, A. Urbano, Molybdenum Oxide Thin Films Obtained by the Hot-Filament Metal Oxide Deposition Technique, Chem. Mater. 16 (2004) 513–520. https://doi.org/10.1021/cm034551a.
[38] N. Cuando-Espitia, J. Redenius, K. Mensink, M. Camacho-López, S. Camacho-López, G. Aguilar, Influence of oxygen pressure on the fs laser-induced oxidation of molybdenum thin films, Opt. Mater. Express, OME. 8 (2018) 581–596. https://doi.org/10.1364/OME.8.000581.
[39] Q. Qu, W.-B. Zhang, K. Huang, H.-M. Chen, Electronic structure, optical properties and band edges of layered MoO3: A first-principles investigation, Computational Materials Science. 130 (2017) 242–248. https://doi.org/10.1016/j.commatsci.2017.01.014.
[40] Y.P. Varshni, Temperature dependence of the energy gap in semiconductors, Physica. 34 (1967) 149–154. https://doi.org/10.1016/0031-8914(67)90062-6.
[41] M. Dieterle, G. Weinberg, G. Mestl, Raman spectroscopy of molybdenum oxides, Phys. Chem. Chem. Phys. 4 (2002) 812–821. https://doi.org/10.1039/B107012F.
[42] M. Łabanowska, Paramagnetic defects in MoO3—revisited, Phys. Chem. Chem. Phys. 1 (1999) 5385–5392. https://doi.org/10.1039/A906194K.
[43] M.A. Reshchikov, Temperature dependence of defect-related photoluminescence in III-V and II-VI semiconductors, Journal of Applied Physics. 115 (2014) 012010. https://doi.org/10.1063/1.4838038.
[44] D.M. Hofmann, B.K. Meyer, H. Alves, F. Leiter, W. Burkhard, N. Romanov, Y. Kim, J. Krüger, E.R. Weber, The Red (1.8 eV) Luminescence in Epitaxially Grown GaN, Physica Status Solidi (a). 180 (2000) 261–265. https://doi.org/10.1002/1521-396X(200007)180:1<261::AID-PSSA261>3.0.CO;2-2.
[45] S.S. Kurbanov, G.N. Panin, T.W. Kim, T.W. Kang, Strong violet luminescence from ZnO nanocrystals grown by the low-temperature chemical solution deposition, Journal of Luminescence. 129 (2009) 1099–1104. https://doi.org/10.1016/j.jlumin.2009.05.005.

[46] H. He, Y. Wang, J. Wang, Z. Ye, Extraction of the surface trap level from photoluminescence: a case study of ZnO nanostructures, Phys. Chem. Chem. Phys. 13 (2011) 14902–14905. https://doi.org/10.1039/C1CP21527B.
[47] D. Cavalcoli, B. Fraboni, A. Cavallini, Chapter Seven - Surface and Defect States in Semiconductors Investigated by Surface Photovoltage, in: L. Romano, V. Privitera, C. Jagadish (Eds.), Semiconductors and Semimetals, Elsevier, 2015: pp. 251–278. https://doi.org/10.1016/bs.semsem.2014.11.004.
[48] S. Balendhran, S. Walia, H. Nili, J.Z. Ou, S. Zhuiykov, R.B. Kaner, S. Sriram, M. Bhaskaran, K. Kalantar-zadeh, Two-Dimensional Molybdenum Trioxide and Dichalcogenides, Advanced Functional Materials. 23 (2013) 3952–3970. https://doi.org/10.1002/adfm.201300125.
[49] N. Illyaskutty, S. Sreedhar, G.S. Kumar, H. Kohler, M. Schwotzer, C. Natzeck, V.P.M. Pillai, Alteration of architecture of MoO3 nanostructures on arbitrary substrates: growth kinetics, spectroscopic and gas sensing properties, Nanoscale. 6 (2014) 13882–13894. https://doi.org/10.1039/C4NR04529G.